Multimodal Imaging of Laser Speckle Contrast Imaging Combined With Mosaic Filter-Based Hyperspectral Imaging for Precise Surgical Guidance

Sanghwa Lee [iD], Jung-Man Namgoong, Youngkyu Kim, Jaepyeong Cha, and Jun Ki Kim [iD]

Abstract—*Objective:* To enable a real-time surgical guidance system that simultaneously monitors blood vessel perfusion, oxygen saturation, thrombosis, and tissue recovery by combining multiple optical imaging techniques into a single system: visible imaging, mosaic filter-based snapshot hyperspectral imaging (HSI), and laser speckle contrast imaging (LSCI). *Methods:* The multimodal optical imaging system was demonstrated by clamping blood vessels in the small intestines of rats to create areas of restricted blood flow. Subsequent tissue damage and regeneration were monitored during procedures. Using LSCI, vessel perfusion was measured, revealing the biological activity and survival of organ tissues. Blood oxygen saturation was monitored using HSI in the near-infrared region. Principal component analysis was used over the spectral dimension to identify an HSI wavelength combination optimized for hemodynamic biomarker visualization. HSI and LSCI were complimentary, identifying thrombus generation and tissue recovery, which was not possible in either modality alone. *Results and Conclusion:* By analyzing multimodal tissue information from visible imaging, LSCI perfusion imaging, and HSI, a recovery prognosis could be determined based on the blood supply to the organ. The unique combination of the complementary imaging techniques into a single surgical microscope holds promise for improving the real-time determination of blood supply and tissue prognosis during surgery. *Significance:* Precise real-time monitoring for vascular anomalies promises to reduce the risk of organ damage in precise surgical operations such as tissue resection and transplantation. In addition, the convergence of label-free imaging technologies removes delays associated with the injection and diffusion of vascular monitoring dyes.

Index Terms—Blood perfusion, blood oxygen saturation, tissue recovery, laser speckle contrast imaging, mosaic filter-based hyperspectral imaging, principal component analysis.

Sanghwa Lee is with Biomedical Engineering Research Center, Asan Medical Center, University of Ulsan College of Medicine, Korea.

Jung-Man Namgoong is with the Department of Surgery, Asan Medical Center, Korea.

Youngkyu Kim is with the Department of Convergence Medicine, University of Ulsan College of Medicine, Korea.

Jaepyeong Cha is with the Sheikh Zyaed Institute for Pediatric Surgical Innovation, Children's National Hospital, Washington, DC 20010 USA (e-mail: jcha2@childrensnational.org).

Jun Ki Kim is with Biomedical Engineering Research Center, Asan Medical Center, University of Ulsan College of Medicine, Seoul 05505, Republic of Korea, and also with the Department of Convergence Medicine, University of Ulsan College of Medicine, Seoul 05505, Korea (e-mail: kim@amc.seoul.kr).

I. INTRODUCTION

SURGICAL resection and transplantations, such as intestinal anastomosis [1], [2] and hepatic parenchymal transection [3], are mainstream therapeutic approaches with significant risks of complication due to blood transfusions. In these surgical procedures, intraoperative blood loss is either directly related to patient survival or is a factor associated with the need for blood transfusion [3]–[5]. Despite red blood cell (RBC) transfusions being necessary to minimize the risk of hemorrhage, improve tissue perfusion, and facilitate oxygenation [3], allogeneic blood transfusion may induce multi-organ failure by activating pro-inflammatory mediators [6], and it has been reported that transfusion increases the rate of complications [7]–[10]. These findings suggest that an operative strategy that minimizes the necessity of blood transfusions is needed to reduce the risk of transfusion reaction.

Techniques for the precise monitoring of blood flow, hemorrhage, and oxygen saturation are thus needed to minimize errors caused by blood vessel ligation, to reduce surgical blood loss, and to successfully isolate and resect ischemic regions. In particular, in the case of intestinal ischemia, vascular occlusion requires bypass anastomosis to restore otherwise irreversible tissue damage and restore the normal flow of ingesta along the

alimentary tract [11]. This suggests that an intestinal model is desirable for demonstrating clinical techniques that minimize the need for transfusion.

Clinical angiography techniques are a promising technique for the assessment of clinical perfusion and, thus, for the minimization of transfusions. In addition to improvements to camera imaging resolution, advances have been made based on a variety of technologies, including ultrasonography [12], fluorescence angiography [13], and computed tomography (CT) [14]. However, ultrasonography and fluorescence angiography require the injection of contrast agents and fluorescent agents, respectively, which take time and planning to inject and spread during surgery. Angiography based on CT and magnetic resonance imaging is difficult to perform simultaneously with imaging and surgery, while repeated exposure to intraoperative X-rays constitutes a significant occupational hazard for surgeons [15]. Therefore, a promising route for improving the success of resection and transplant surgeries may be the development of optical angiography devices that integrate with existing surgical microscopes for real-time imaging of blood flow, tissue oxygenation, and tissue health without requiring contrast agent.

Laser speckle contrast imaging (LSCI) is a noninvasive real-time imaging technology that enables the visualization of blood flow without requiring the use of phosphors or contrast agents. This technique uses a high-speed and high-resolution camera to detect variations in laser speckle scattering caused over time by the motion of scattering centers such as RBCs [16], [17]. LSCI is low cost, easy to implement, provides simultaneous high spatial and temporal resolution, and has been applied to a variety of biological imaging domains, including dermal blood flow [18], mouse cochlea [19], retinal vasomotion [20], and the deep brain [16]. The LSCI method has been used for real-time surgical microscope guidance to minimize damage during organ transplantation and removal, and to determine the survival prognosis of transplanted organs by verifying tissue blood perfusion [21], [22]. However, LSCI alone, without information on oxygen saturation, blood clotting, or tissue necrosis, is limited in its ability to assist transplant organ survival and prognosis. To overcome this limitation, synchronized hyperspectral imaging (HSI) devices can be applied as tools for multi-signal, non-labeled imaging for successful transplantation guidance [23]–[25].

Hyperspectral imaging is another promising imaging modality for optical angiography. By capturing intensity information at each pixel coordinate across many wavelength bands other than the standard red, blue, and green (RBG) colors, increased insight may be derived into tissue oxygenation and blood perfusion. As the absorption, reflection, and scattering of biological samples depend on the chemical properties of the sample in a wavelength-dependent manner, images obtained from additional spectra as in HSI include information on biological sample composition that is challenging to obtain using color cameras or the human eye [25]–[30]. In particular, HSI has recently been shown to improve surgeon identification of transection margins during colon resection [30], and its noninvasive imaging of blood perfusion has proven informative for a variety of clinical applications, including early detection of flap perfusion problems [31], cutaneous wound assessment [32], and the assessment of diabetic foot wounds [33].

There are a multitude of methods to achieve HSI and to perform analysis of the associated spectral datacubes. In bioimaging, sequential (scanning) methods have been applied using devices such as filter wheels [34]–[37], liquid crystal tunable filters (LCTF) [38]–[40], and acousto-optic tunable filters (AOTF) [41], [42], but these methods require significant time to acquire single frames. More recently, snapshot HSI sensors have been commercialized which capture entire spectral domains at once [25], [27], [42]. Mosaic filter sensors, specifically, reduce the size of the datacube to that which can be captured on a single imaging sensor, enabling the real-time capture and processing of hyperspectral information. However, these smaller datacubes have reduced spatial resolution and a discrete number of spectral filters, leaving them with low resolution for surgical guidance. As a result, the combination of LSCI and HSI is a promising way to improve the measurement of both tissue oxygenation and perfusion in surgery [27], [38], [43]–[47]. Furthermore, both LSCI and HSI can be easily combined with both endoscopy and microscopy [23], [48], [49].

Despite several recent examples of the synergistic combination of LSCI and HSI in preclinical experiments, the demonstration of this multimodal imaging for realistic surgical imaging has been limited. Previous demonstrations have been limited to dermal imaging [43]–[45], optically cleared tissue [38], [46], or implanted glass windows [47].

This study combines visible, LSCI, and snapshot HSI cameras into a single clinical multimodal imaging device suitable for real-time intraoperative visualization and demonstrates such a device in a surgical model for the first time, to the best knowledge of the authors. The capabilities of each component of the system are demonstrated in a rat intestinal ischemia model, with LSCI determining blood perfusion and dual HSI cameras distinguishing tissue from blood vessels, detecting oxygen saturation, and highlighting hemorrhages which are difficult to distinguish in RGB imaging. These modalities are combined simultaneously and synchronously with visible imaging, as shown in Fig. 1. The application of a mosaic filter HSI sensor enables real-time label-free imaging. The convergent device shows promise for the practical early detection and prevention of complications in surgical transplantation and removal procedures.

II. METHODS

A. Rat Anesthesia and Intestinal Exposure

Male and female Sprague-Dawley rats (n = 4) were purchased from Charles River Laboratories (Wilmington, Massachusetts, USA). Immediately before the experiment, the weights of the rats ranged from 275 to 285 g. The rats were administered 3% isoflurane for three minutes and then 80 mg/kg ketamine and 5 mg/kg xylazine for anesthesia after sedation and restraint. The entire experiment was performed under 1% isoflurane inhalation. A midline laparotomy was performed and the partially exposed small intestine was placed under our system for imaging. As shown in Fig. S1, images were captured after spreading the exposed small intestine on a blue surgical paper towel to minimize signal interference from exposed tissues other than the small intestine. All animal experiments followed guidelines
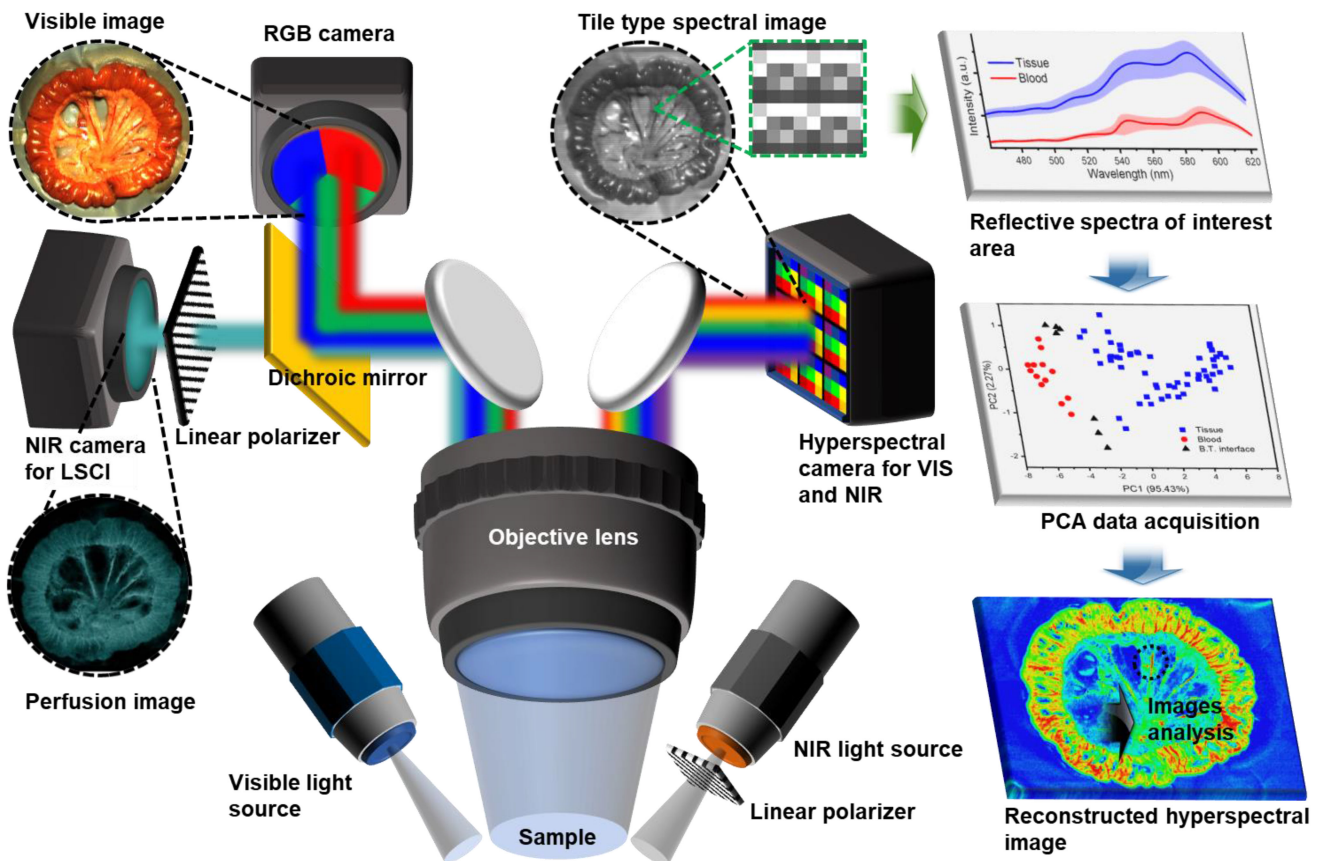
Fig. 1. Schematic diagram of a visible imaging, LSCI, and HSI system integration device for surgical image guidance with spectrum and PCA results obtained from spectral tile mosaic cameras and the demonstrated image analysis process based on spectral reconstruction. LSCI: laser speckle contrast imaging; HSI: hyperspectral imaging; NIR: near-infrared; RGB: red, green, and blue; VIS: visible; PCA: principal component analysis.

(#30597) and protocols approved by the institutional animal care and use committee of the Asan Institute for Life Sciences, Asan Medical Center (2019–02-093), under the laws of the Republic of Korea.

B. Installation of the Multi-Imaging Device in a Surgical Microscope

A surgical ophthalmic microscope (OPMI S5, Carl Zeiss, Germany) with oblique illumination was introduced for the obtainment of synchronized biometric images by combining a color imager (RGB), LSCI, and hyperspectral multi-imaging devices. The microscope (Zeiss OPMI S5 Microscope) delivers images from the main objective lens with a 250-mm focal length. Illumination was provided over the oblique illumination channel using a halogen lamp (Zeiss 304950 Emergency Halogen Bulb: 100W 12V) and an 830-nm laser diode (P = 5 mW, Wuhan, China) for speckle pattern generation. The microscope provides two camera ports via a beam splitter in front of the eyepiece. For our application, one port (the left port in Fig. S1) was connected to bright-field and LSCI cameras, while the other port (the right port in Fig. S1) was connected to hyperspectral cameras. The high-resolution bright-field (30 fps, HD Color Vision, GS3-U3-41C6C-C; FLIR, Wilsonville, OR, USA) and

LSCI (90 fps, NIR LSCI, GS3-U3-41C6NIR-C, FLIR) cameras had a resolution of 2048×2048 pixels. These were connected to a 50:50 beam splitter coupler (Carl Zeiss, Germany). For LSCI of the near-infrared (NIR) region, a laser line-filter (830 nm cut) was used. To calculate speckle contrast analysis, we used a 5×5 pixel window spatial filtering with 10 temporal averaging to enhance both temporal and spatial resolutions. The imaging process, setup, and performance of LSCI compared with those of fluorescence imaging have been previously demonstrated [42]. There are also prior studies of validation through fluid chip-based vascular mimic phantoms [50].

C. Hyperspectral Camera Installation and Image Analysis

The hyperspectral camera used in this study was a mosaic filter-type spectral image measurement device comprising two hyperspectral cameras, one visible (VIS) (10 fps, MQ022HG-IM-SM4x4-VIS, XIMEA, Münster, Germany) and one NIR (10 fps, MQ022HG-IM-SM5x5-NIR, XIMEA), which were combined to visualize the same spatial region in different spectral ranges using a dichroic mirror. The VIS and NIR hyperspectral cameras each had 2048 pixels $\times$ 1088 pixels. The VIS camera captured 16 wavelengths on 4×4 mosaic filter

tiles for 512×272 image resolution, while the NIR camera fit 25 wavelength filters into 5×5 mosaic pixels, for 409×217 resolution video. The mosaic pixels tiled the image sensor and wavelength filters were placed on each mosaic pixel in an arbitrary but fixed arrangement, with the center wavelength of each filter shown for a single pixel of the VIS and NIR cameras in Figs. S2a and S2b, respectively. The VIS wavelengths fell in the range of 460 and 630 nm, while the NIR wavelengths were between 600 and 870 nm. Fig. S3a shows a raw hyperspectral VIS image with the concurrently captured RGB image inset. The reconstructed spectra of two arbitrary regions (blue, red) from the hyperspectral image are shown in Fig. S3b. A reference spectrum was assembled to refer to the relative value of the quantum efficiency for each spectrum of the light source, internal filter, and hyperspectral camera. Conversion of the spectral intensities in the visible $I(x_1, y_2, \lambda_{1 \sim 16})$ and infrared $I(x_2, y_2, \lambda'_{1 \sim 25})$ regions from hyperspectral raw images to multidimensional arrays was performed in MATLAB. Principal component analysis (PCA) of the hyperspectral information was performed using XLSTAT 2018 software. Graphs were plotted using Origin 2018, and imaging of the results based on statistical analysis was performed using the Origin 2018 image mapping tool.

III. Results

A. Dimensionality Reduction for Vessel Finding in Hyperspectral Images

Raw hyperspectral image data were provided from the camera as black and white images, wherein each pixel represents the intensity of a narrow wavelength band measured from a specific part of the mosaic. The mosaic spectral filter layout within each pixel and the raw image data are shown in Figs. S2 and S3. In the standard RGB color image of Fig. 2(a), blood vessels appear reddish compared with their surroundings due to the densely oxygenated red blood cells that absorb light in the blue and green wavelengths [51]. In contrast, as shown in Fig. 2(b), the blood vessels in the raw hyperspectral image of the same region appear darker than the surrounding tissue for most wavelengths. These absorption data contain more information than the absorption ratio of just the blue and green wavelengths. The average spectrum of the region inset in Fig. 2(b) is plotted in Fig. 2(c) from 460 to 630 nm. The average value and one standard deviation are depicted as solid lines and light bands, respectively. Most of the variation appears to be distributed between 530 and 620 nm. However, since the differences between the vessel and the surrounding tissue spectra extend over the entire spectral domain, PCA was performed using each wavelength as a domain variable, to find an alternative basis (the PCs) of domain variables that sequentially maximize the data variance [52]. Using the data converted to $I(x_1, y_2, \lambda_{1 \sim 16})$ of the hyperspectral image, $\lambda_{1 \sim 16}$ of the data unit corresponding to each (x_1, y_2) were set as variables and plotted in the PC space. As shown in Fig. 2(d), 95.43% of the total data variability was accounted for by the first principal component (PC1), along which the blood vessels (red) and surrounding tissues (blue) were separated successfully. When HSI superpixels were categorized PCA, the pixels that were difficult to categorize lay
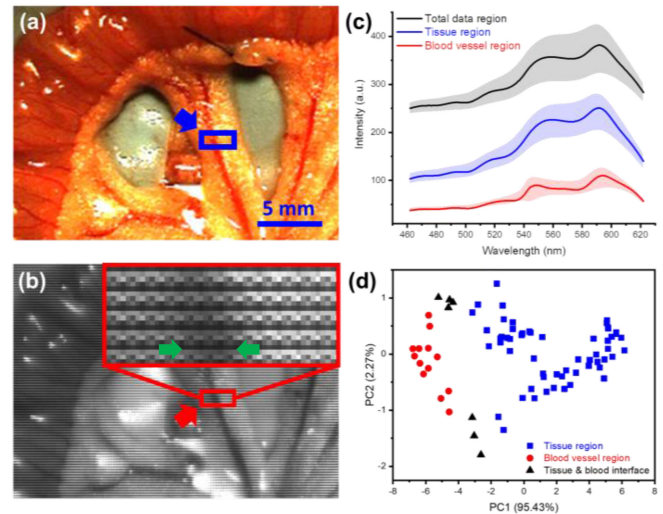

Fig. 2. Partitioning of acquired images into tissue and vasculature by hyperspectral analysis. The synchronized (a) RGB and (b) raw HSI images show the indicated ROI. The magnified ROI (inset) shows the tiling of the spectral filters. Green allows indicate the blood-tissue boundary. (c) Plots of average spectra (solid lines) reconstructed from HSI with standard deviations (shaded) showing different spectral characteristics within the ROI and (d) clear separation of tissue and vascular signals by PCA. HSI: hyperspectral imaging; RGB: red, green, and blue; PCA: principal component analysis; ROI, region of interest.

on the blood-tissue boundary, for which the tissue spectrum varies across the pixel. When displayed in PC space, these pixels formed the two groups of black triangles shown in Fig. 2(d). The second principal component (PC2) separated these points; the group with a positive PC2 component consisted of pixels from the tissue-blood vessel boundary with tissue on the left, while the group with a negative PC2 component consisted of points from the boundary on the other side of the blood vessel. The successful separation of blood vessels from surrounding tissues in PC space is thus evident. In addition, the variability of PCA over time of the spectral signal obtained from blood vessels using the mosaic-based HSI used in this study is shown in Figure S3c. As shown in Figure S3d, the spectra were compared for inter-animal differences, and it was confirmed that they are of similar shapes. However, there appears to be a difference in PCA space according to the brightness of the lighting between animals (Fig. S3e). Normalization to 462 nm results in overlapping of the data distribution as shown in Fig. S3f. Therefore, the difference in inter-animal data distribution is also within the range of variation over time.

B. Intestinal Occlusion and Blood Vessel Localization

While RGB data representations lend naturally to color image generation, color images of hyperspectral data should be based on the optimal representation of the data. Depending on the application, optimal false color channels for imaging may be based on a narrowband region in which one wavelength is selected, or may be based on the relative intensities between wavelengths. If the target material selectively absorbs or reflects a single wavelength, then clinical imaging may be possible
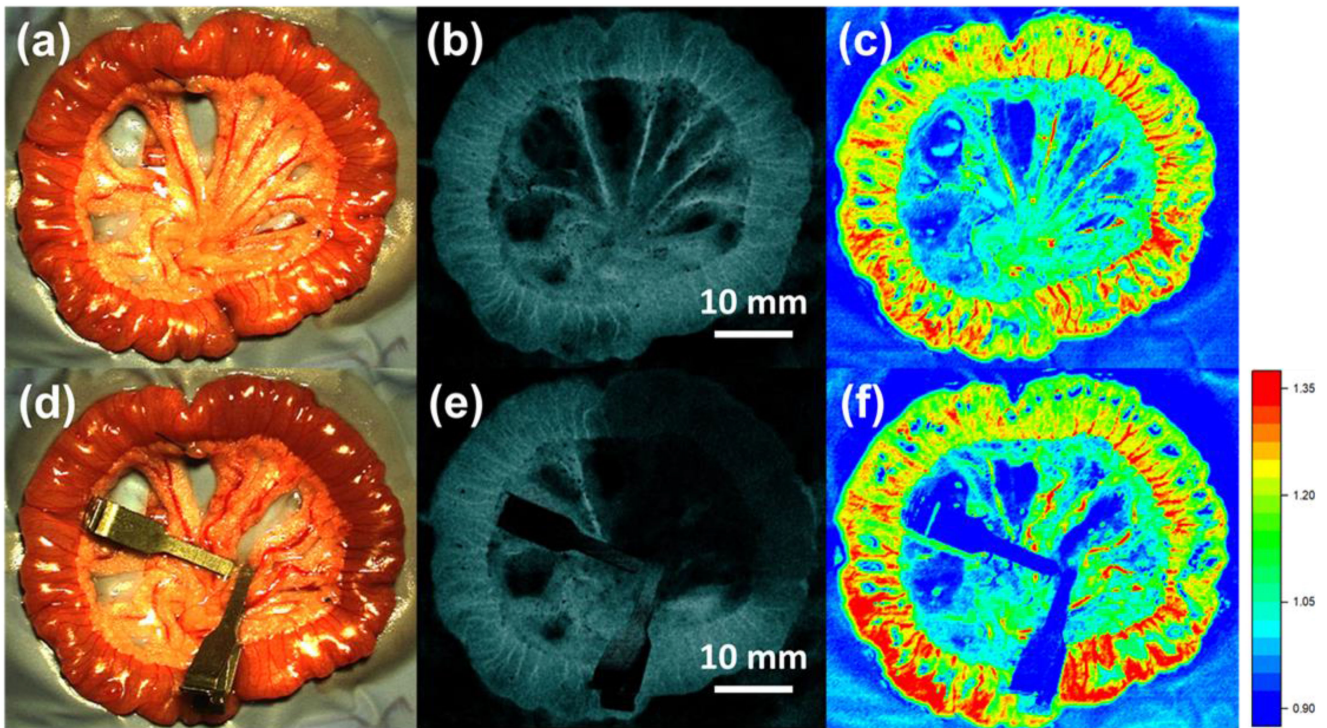
Fig. 3. Integrated imaging measurements of restricted blood flow in the intestines of anesthetized rats. (a), (d) Standard color image, (b), (e) LSCI showing blood perfusion and (c), (f) HSI showing reconstruction of blood distribution (a)–(c) before and (d)–(f) after blood flow clamping. Control of blood flow was enabled by ligating with the sutures (in white circles) before clamping. LSCI: laser speckle contrast imaging; HSI: hyperspectral imaging.

from a single narrow band; however, in most cases, contrast is improved by combining intensities from two or more wavelengths. In addition, since the local image intensity may vary depending on surface geometry and illumination conditions, image formation based on relative spectral signals may result in much loss of the difference in the local signal intensities. For example, shadows of wrinkles on the organ surface may form nonuniform illumination L(x,y); in this case, the HSI image may take the form I (x, y, λ_a) = L (x, y) × I '(λ_a).

To distinguish between blood vessels and surrounding tissues and to identify specific vasculature, the HSI images were reconstructed as shown in Fig. 3, using wavelengths selected from the spectral PCA results in Fig. 2 and the absorption spectra of hemoglobin. The heatmap was plotted using the following reconstruction method according to the selected site of blood vessels or surrounding tissues.

$$I_{x,y} \text{ (selected site)} = \frac{\sum_{\lambda_1} I_{x,y}(\lambda_1)}{\sum_{\lambda_2} I_{x,y}(\lambda_2)}, \tag{1}$$

where λ_1^{blood} = (592, 603, 615), λ_2^{blood} = (555, 570, 581), $\lambda_1^{\text{tissue}}$ = (570, 592, 603), $\lambda_2^{\text{tissue}}$ = (462, 469, 482). The HSI image was colored with a heat map of the signal intensity, as shown on the right side of the image. Fig. 3(a)–(c) show synchronized RGB, LSCI, and HSI images of the anesthetized rat intestine, respectively, while Fig. 3(d)–(f) show the same organ immediately after clamping several blood vessels. Before and after blood vessel occlusion, the vessels were ligated with

sutures, as shown in the white circles in Fig. 3(a), allowing the blood flow to be switched by clamping. As shown in Fig. 3(b) and (e), the LSCI image of the restricted area after clamping appears dark as the blood flow is occluded. In contrast, regardless of the flow of blood, the HSI images in Fig. 3(c) and f show the locations of all blood vessels (except the area obscured by the clips).

C. Visualization of Oxygen Saturation Using HSI

Perfusion-free localization of blood vessels and imaging of perfusion are key factors for determining the prognosis of transplanted organs after vascular anastomosis. More direct information is obtained by confirming normal bioactivity through oxygen saturation monitoring. Absorption in the 600-800 nm wavelength range is indicative of the oxygen saturation of hemoglobin [51], [53].

Fig. 4(a) and (b) show regions of blood vessels with both free and clamped flows. The spectrum was monitored for changes in the region indicated by the white dotted line in the figure, and the signal change over time was recorded from 600 to 870 nm, as shown for the clamped region in Fig. 4(c).

Relative signal intensities for 590–620 nm versus 550–585 nm were used to reconstruct blood vessel images from the hyperspectral data. This representation seems more suitable for imaging the hemoglobin distribution than for imaging blood vessels. As shown in the dashed circles of Fig. S4a to c, leaking blood appears similar to blood in vessels in RGB camera images
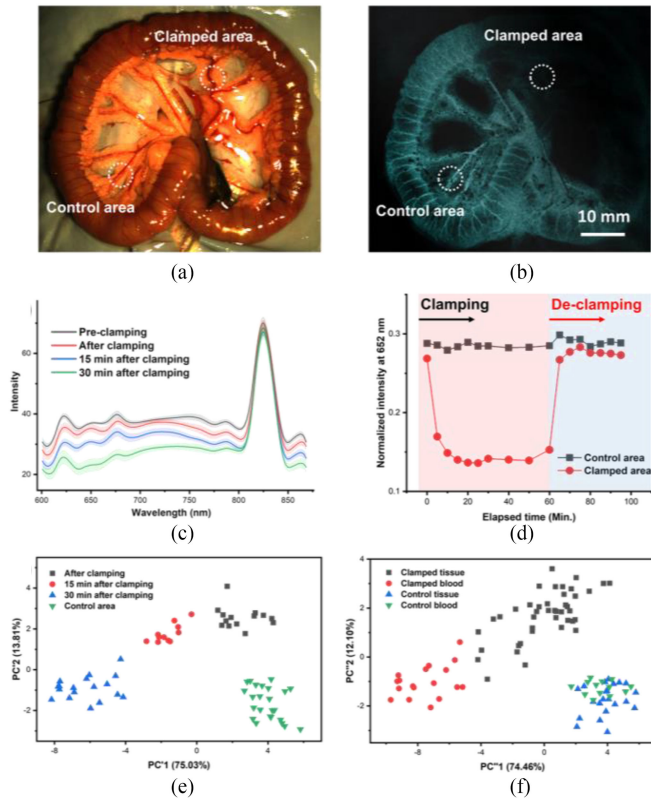
Fig. 4. Results of using a hyperspectral camera in the NIR region to measure changes in oxygen saturation for long-term clamping. (a) Visible image and (b) LSCI image showing the data acquisition area (dashed circle) for clamping analysis. (c) Change in the average spectrum and standard deviation (shadow near the line) over time in the NIR spectral region after occlusion. (d) Comparison of light intensity change according to clamping and declamping with the control area. PCA results for a group of data according to clamping (e) time and (f) location. LSCI: laser speckle contrast imaging; NIR: near-infrared; PCA: principal components analysis.

and in LSCI images. However, in HSI the intensity of leaking blood is greater than that of the adjacent vessels.

Over time, the signal amplitude decreased in the spectral region related to hemoglobin oxidization. Monitoring of the target area in 15-minute increments showed a uniform and narrow standard deviation of the average spectrum, indicating low variation between measurements. In addition, as shown in Fig. 4(d), following declamping the 632 nm signal intensity, which is associated with heme oxygen saturation, returned to the same level as that of the control blood vessels.

PCA was also used to monitor the time and perfusion dependencies of the spectra. A change in spectra observed in 15-minute intervals after occlusion appeared in PC space as bunching and negative dependence in PC1 (75.83%). These observed changes confirmed that the oxygen saturation of blood vessels can be monitored using an HSI camera in the NIR region. However, while it is possible to confirm the hemodynamics using a hyperspectral camera in the NIR region, it is generally difficult to distinguish blood vessels and surrounding tissues in the NIR region. As shown in Fig. 4(f), the spectral components of the blood vessels and surrounding tissues were not separated well until oxygen depletion occurred due to occlusion.
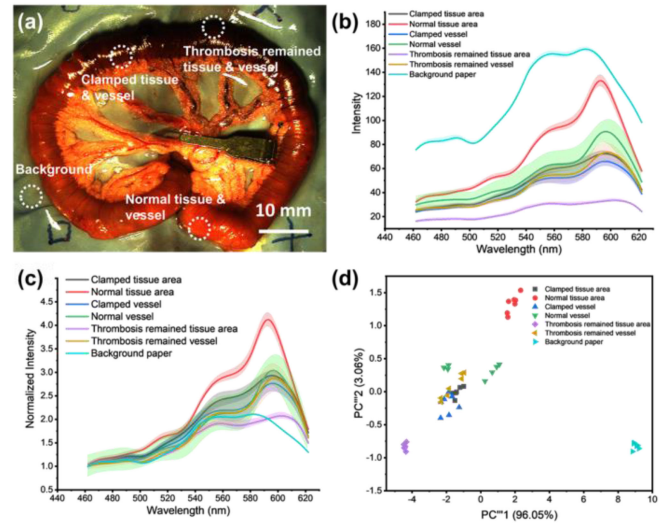

Fig. 5. (a) Data acquisition regions for background, normal, clamped, and thrombotic tissues and blood vessels to confirm signal changes due to long-term thrombosis and reperfusion. (b) Average spectra and standard deviations of the selected regions as reconstructed from HSI. (c) Signal graphs normalized at 460 nm form the basis for relative wavelength intensity imaging. (d) Spectral PCA results for the analysis of the imaging groups. HSI: hyperspectral imaging; PCA, principal components analysis.

D. Monitoring of Thrombosis and Tissue Spectra After Blood Reperfusion

Thrombosis often occurs due to coagulation after surgery and trauma. Thrombi impede the supply of nutrients and oxygen to tissues by blocking blood circulation, resulting in necrosis and dysfunction [54]. Even when blood flow is present, stagnant blood may clot due to low flow rates, causing potentially fatal complications [55], [56]. Therefore, in addition to visualizing blood oxygenation as demonstrated above, monitoring of thromboses and changes in tissue metabolism during perfusion and reperfusion in the small intestine could be important in determining the prognosis for tissue recovery. While under monitoring by the integrated RGB, LSCI, and HSI system, blood flow through part of the small intestine of the rat was blocked for one hour, after which the tissue was left to reperfuse for one hour. As shown in Fig. 5(a), the average spectra and their standard deviations were compared between the paper background and between regions of tissue and blood vessels in their normal, clamped, and released (persistent thrombotic) states over the course of the obstruction and subsequent reperfusion (Fig. 5(b) and (c)). As in the vascular HSI image shown in Fig. 3, reconstruction was performed by applying PCA on the vascular and tissue characteristics. An image of the tissue was formed from the ratio signal intensities from the 570–605 nm range to the 460–485 nm range; when the blood supply was stopped or reperfusion was not performed, the image intensity dropped accordingly. As shown in Fig. 5(d), the difference in the graph of each region was plotted through PCA, and tissue-related data were grouped separately. On the other hand, the blood vessel-related data groups are not well separated, but changes in blood vessel status were
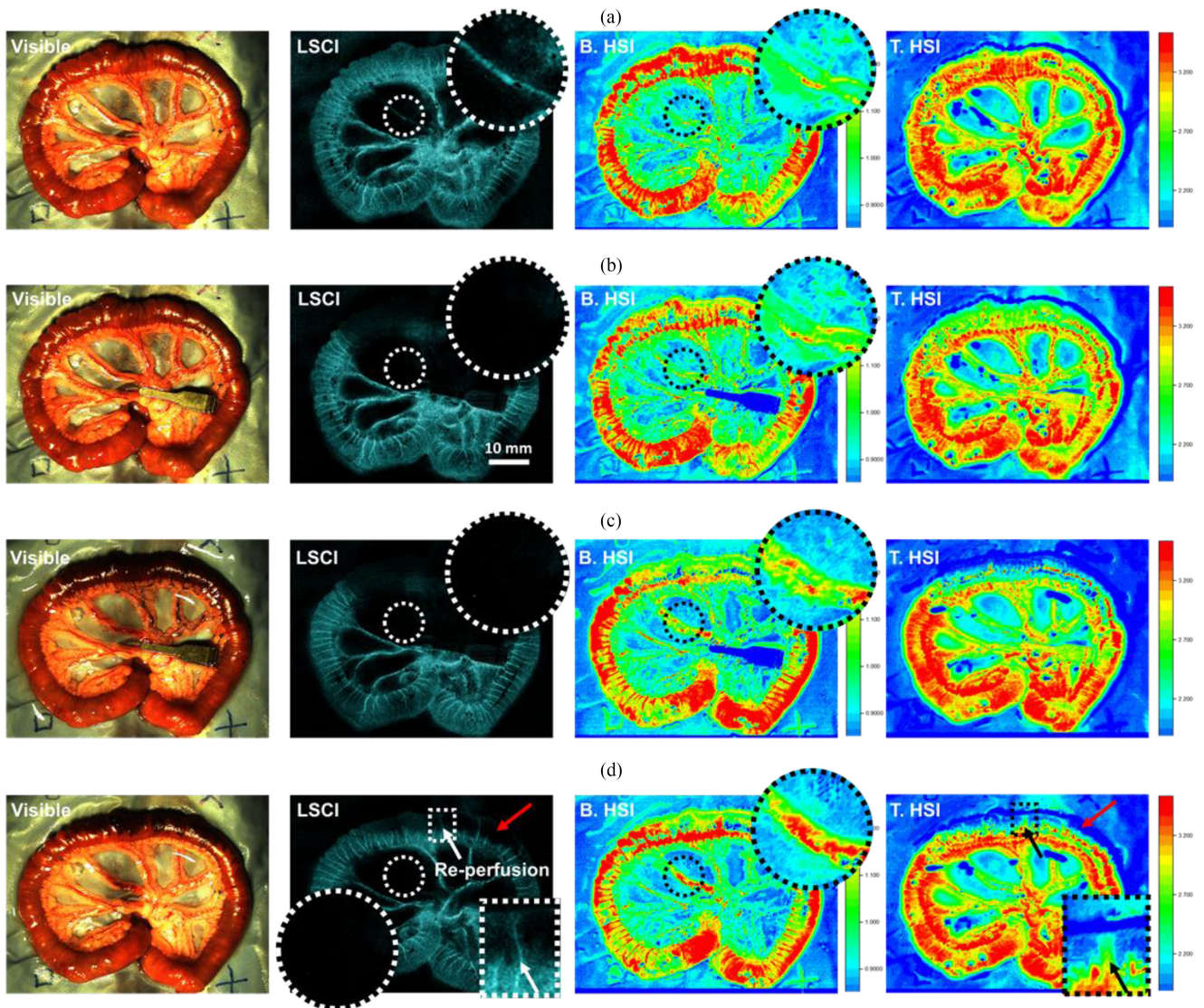
Fig. 6.   Synchronized visible, LSCI, blood-specified HSI (B. HSI), and tissue-specified HSI (T. HSI) images as blood flow is controlled by clamping. (a)–(b) Image sets of a comparison group before clamping (a) and a rat intestine where blood perfusion is closed immediately after clamping (b). (c)–(d) Image sets in which thrombus and intestinal tissue damage occurred 1 h after clamping (c), and confirmation of tissue reperfusion and thrombus 1 h after declamping (d). The white and black arrows indicate areas where tissue has recovered from reperfusion, the red arrows indicate areas of tissue that have not recovered, and the dashed circles indicate areas where thrombus monitoring has been confirmed. The dotted circled and squared areas were enlarged three times and inserted as insets, respectively. LSCI: laser speckle contrast imaging; HSI: hyperspectral imaging.

confirmed with the support of the LSCI and oxygen saturation results shown above.

This trend is shown in Fig. 6, in which images obtained during the clamping and declamping process were synchronized. Blood-specific HSI reconstruction (B. HSI) and tissue-specific HSI reconstruction (T. HSI) are shown. As shown in Fig. 6(d), one hour after declamping, the region in which reperfusion occurred in the LSCI (white arrow) and the portion where blood reperfusion did not occur (red arrow) are clearly distinguishable in T. HSI and LSCI. In addition, as shown in the dotted circle in Fig. 6, some blood vessels visible in LSCI before clamping disappeared during and after declamping. On B. HSI, the signal intensity increased as blood accumulated in the blood vessel inlet where flow on the LSCI was stopped (Fig. 6(c)–(d)).

Depending on the condition of the remaining thrombus, the area that prevents reperfusion and inhibits tissue recovery is clearly revealed through this multimodal imaging. The results of this study demonstrated complementary analysis through imaging by a standard surgical microscope and may provide surgeons with insight into improving the prognosis for localized thrombolysis and the excision of metabolism-deficient tissues.

IV. DISCUSSION

Currently, minimization of bleeding during surgical excision and transplantation procedures is ensured by ligating blood vessels around the ablation and translation sites. However, ensuring adequate blood supply to tissues is also an important

consideration. This study used a rat model wherein intestinal blood flow was controlled to demonstrate the efficacy of the multimodal imaging device in observing tissue blood supply and recovery prognosis after transplantation. To acquire blood flow and tissue signals, the system synchronized images between an RGB camera, an LSCI camera, and two HSI cameras, which were integrated into a surgical microscope. From the raw hyperspectral image, the signal intensity for each wavelength was converted to a spectral intensity profile. An enhanced contrast factor was obtained from analysis of tissue and blood vessel differences of averages, while PCA was demonstrated to be effective in creating a basis by which pixels could be easily classified.

Datacube minimization and spectral calibration are significant requirements for real-time HSI analysis [25]. Although the snapshot HSI sensors used in this paper generate less data per frame than other HSI techniques, by PCA and manual registration of obvious target and control regions, it is possible to reduce dimensionality in a manner independent of absolute spectral intensities, thus simplifying both display and analysis. The variability of the spectrum obtained from this mosaic-based snapshot HSI is provided in Fig. 2 and Fig. S3. Therefore, it was confirmed that this technique is accurate in monitoring spectral changes during vascular ligation for resection and ischemic bowel disease. The need for absolute calibration targets is overcome, as the wavelength regions identified for vessel recognition via PCA overlap with the well-known absorption bands of hemoglobin. Similar to previous demonstrations of HSI for determining oxygen saturation, PCA also reveals the optimized (combinations of) wavelengths that maximize the data variance, clearly distinguishing vasculature and perfusion.

In addition, hemodynamic biomarker imaging was performed based on the relative signal intensities between HSI wavelengths and the visible absorption wavelength of deoxygenated hemoglobin [26]. However, HSI only provides static information, although inertia for recovery is estimated through the combination with LSCI, which provides dynamic information. Images vividly capturing the distributions of blood flow during the clamping of rat intestine blood vessels were obtained by synchronizing the visible images for blood, LSCI images of perfusion images, and blood distribution obtained from hyperspectral images.

Hyperspectral vascular images were generated based on the relative signal intensities between wavelengths and were displayed such that local brightness variation was minimized while maximizing the target tissue signal. In addition, blood vessel oxygen saturation was visible in the infrared HSI, with the characteristic absorption of saturated hemoglobin decreasing over time in the area of clamped blood flow and returning to the baseline after the clamps were released. PCA was used to detect systematic changes between spectra from tissue and blood vessels in the NIR region and their dependence on the oxygen saturation with time and clamping. Direct imaging of thrombus occurrence and tissue variation during guided surgery was demonstrated through the integrated imaging system. LSCI tuned for tissue-specific signals in the optimized spectral basis confirmed the loss of tissue-specific signals where reperfusion did not occur, while blood-specific optimization revealed pooling in thrombotic regions. Thus RGB imaging, LSCI, and HSI were integrated to provide direct diagnostic data for surgical guidance, including blood perfusion, distribution, oxygen saturation, thrombus formation, and tissue recovery prognosis. Furthermore, the conventional oxygen saturation monitoring method monitors the average change in the body, whereas local oxygen saturation monitoring through the hyperspectral method monitors the organ's own oxygen saturation during surgical treatment such as organ transplantation, resection, or vascular anastomosis. Local oxygen saturation imaging of PO2 through HSI has been applied to the skin [57], but in this study, it was added to the monitoring of vascular dynamics such as thrombus and perfusion for prognosis, which greatly contributed to the surgical guide.

Several similar systems have been demonstrated that combine LSCI, HSI, and sometimes RGB imaging to measure the perfusion and oxygen saturation of clinically relevant tissues. LSCI and multispectral imaging were used by White et al. [47] to assess tissue perfusion in mice via a glass window as early as 2012, while Ren et al. characterized wound tissue [44]. Zhang et al. integrated an IR imager, LSCI, and VIS-NIR HSI (linear scan) to characterize wound healing, with image registration to track wounds over a period of 28 days to quantify tissue perfusion and show its correlation with heat emission [43]. However, these methods were demonstrated on skin or skin folds, which limits their practicality for clinical imaging and surgery. Feng et al. have combined LSCI and visible HSI into a single device to demonstrate optical clearing of the mouse cranium [38] and the perfusion and saturation in mouse models of diabetes [46]. While the structure of their system was quite similar to that demonstrated here, their method was limited to visible wavelengths and high frame-rates were not accessible due to the use of LCTF-based HSI.

In the clinical application of the existing LSCI and HSI systems, factors that induce blurring of images need to be considered, such as breathing and heartbeat. If the image acquisition speed is faster than the movement of the subject, this blurring phenomenon is reduced. There are literature addressing the motion artifacts such as breathing and heartbeats by introducing a software algorithm to compensate. The motion artifacts can be further mitigated by heart-beat triggered image processing [58], [59]. The image performance was confirmed through a video of LSCI and mosaic-HSI used in this study (Supplementary Materials). Although the technology detailed in this paper is practical and ready for clinical application, many further studies have been performed on LSCI and HSI systems in order to assess the limits of their clinical application. The fundamentally noninvasive nature of this technology and its non-interfering, synergistic impact on existing clinical tools suggests that there is little reason to delay small-scale clinical trials.

V. CONCLUSION

A new system has been presented for simultaneous assessment of blood leakage, perfusion, and oxygenation in the surgical field during transplantations. The system combines an

RGB camera, an LSCI camera, and two HSI cameras, which were integrated into a surgical microscope. The complementary imaging techniques of HSI, LSCI, and visible imaging provide information that may inform surgical and clinical decisions and treatment planning, as demonstrated in a rat model of intestinal ischemia. With minimal calibration and without labeling or contrast agents, dimensional reduction via PCA allows HSI data to be transformed into images, distinguishing tissue from blood vessels, hemorrhagic tissue from perfused tissue, and oxygenated blood from hypoxic blood. Meanwhile, LSCI provides real-time insight into blood flow and occlusion. Through the use of this integrated, clinically-ready imaging device, it may be possible to reduce the risk inherent in organ tissue excision and transplantation, enable precise surgery, and predict postsurgical prognosis.

References

[1] Y. H. Ho and M. A. T. Ashour, "Techniques for colorectal anastomosis," *World J. Gastroenterol.*, vol. 16, no. 13, pp. 1610–1621, Apr.–Jul. 2010, doi: 10.3748/wjg.v16.i13.1610.

[2] L. Yao *et al.*, "An effective new intestinal anastomosis method," *Med. Sci. Monitor*, vol. 22, pp. 4570–4576, Nov. 2016, doi: 10.12659/Msm.902000.

[3] N. Latchana *et al.*, "Red blood cell transfusion in liver resection," *Langenbeck Arch. Surg.*, vol. 404, no. 1, pp. 1–9, Feb. 2019, doi: 10.1007/s00423-018-1746-2.

[4] T. Kamei *et al.*, "Intraoperative blood loss is a critical risk factor for peritoneal recurrence after curative resection of advanced gastric cancer," *World J. Surg.*, vol. 33, no. 6, pp. 1240–1246, Jun. 2009, doi: 10.1007/s00268-009-9979-4.

[5] Y. X. Liang *et al.*, "Impact of intraoperative blood loss on survival after curative resection for gastric cancer," *World J. Gastroenterol.*, vol. 19, no. 33, pp. 5542–5550, Sep. 2013, doi: 10.3748/wjg.v19.i33.5542.

[6] E. C. Vamvakas and M. A. Blajchman, "Transfusion-related immunomodulation (TRIM): An update," *Blood Rev.*, vol. 21, no. 6, pp. 327–348, Nov. 2007, doi: 10.1016/j.blre.2007.07.003.

[7] G. Gozzetti *et al.*, "Liver resection without blood transfusion," *Brit. J. Surg.*, vol. 82, no. 8, pp. 1105–1110, Aug. 1995, doi: 10.1002/bjs.1800820833.

[8] J. Hallet *et al.*, "The impact of perioperative blood transfusions on short-term outcomes following hepatectomy," *Hepatobiliary Surg. Nutr.*, vol. 7, no. 1, pp. 1–10, Feb. 2018, doi: 10.21037/hbsn.2017.05.07.

[9] D. A. Kooby *et al.*, "Influence of transfusions on perioperative and long-term outcome in patients following hepatic resection for colorectal metastases," *Ann. Surg.*, vol. 237, no. 6, pp. 860–870, Jun. 2003, doi: 10.1097/01.SLA.0000072371.95588.DA.

[10] S. E. Tevis and G. D. Kennedy, "Postoperative complications: Looking forward to a safer future," *Clin. Colon Rectal Surg.*, vol. 29, no. 3, pp. 246–252, Sep. 2016, doi: 10.1055/s-0036-1584501.

[11] M. Bala *et al.*, "Acute mesenteric ischemia: Guidelines of the world society of emergency surgery," *World J. Emerg. Surg.*, vol. 12, Aug. 2017, doi: 10.1186/s13017-017-0150-5.

[12] C. Errico *et al.*, "Ultrafast ultrasound localization microscopy for deep super-resolution vascular imaging," *Nature*, vol. 527, no. 7579, pp. 499–502, Nov. 2015, doi: 10.1038/nature16066.

[13] T. H. Degett, H. S. Andersen, and I. Gogenur, "Indocyanine green fluorescence angiography for intraoperative assessment of gastrointestinal anastomotic perfusion: A systematic review of clinical trials," *Langenbeck's Arch. Surg.*, vol. 401, no. 6, pp. 767–775, Sep. 2016, doi: 10.1007/s00423-016-1400-9.

[14] G. Bastarrika *et al.*, "Coronary CT angiography: Applications," *Radiologic Clin. North Amer.*, vol. 47, no. 1, pp. 91–107, Jan. 2009, doi: 10.1016/j.rcl.2008.10.010.

[15] R. A. Hayda *et al.*, "Radiation exposure and health risks for orthopaedic surgeons," *J. Amer. Acad. Orthopaedic Surgeons*, vol. 26, no. 8, pp. 268–277, Apr. 2018, doi: 10.5435/JAAOS-D-16-00342.

[16] M. Chen *et al.*, "Laser speckle contrast imaging of blood flow in the deep brain using microendoscopy," *Opt. Lett.*, vol. 43, no. 22, pp. 5627–5630, Nov. 2018, doi: 10.1364/Ol.43.005627.

[17] S. C. Gnyawali *et al.*, "Retooling laser speckle contrast analysis algorithm to enhance non-invasive high resolution laser speckle functional imaging of cutaneous microcirculation," *Sci. Rep.*, vol. 7, Jan. 2017, doi: 10.1038/srep41048.

[18] G. Mahe *et al.*, "Laser speckle contrast imaging accurately measures blood flow over moving skin surfaces," *Microvascular Res.*, vol. 81, no. 2, pp. 183–188, Mar. 2011, doi: 10.1016/j.mvr.2010.11.013.

[19] T. H. Kong *et al.*, "Monitoring blood-flow in the mouse cochlea using an endoscopic laser speckle contrast imaging system," *Plos One*, vol. 13, no. 2, Feb. 2018, doi: 10.1371/journal.pone.0191978.

[20] A. Y. Neganova *et al.*, "Rat retinal vasomotion assessed by laser speckle imaging," *Plos One*, vol. 12, no. 3, Mar. 2017, doi: 10.1371/journal.pone.0173805.

[21] S. M. Jansen *et al.*, "Can we predict necrosis intra-operatively? Real-time optical quantitative perfusion imaging in surgery: Study protocol for a prospective, observational, in vivo pilot study," *Pilot Feasibility Stud.*, vol. 3, no. 1, Dec. 2017, Art. no. 65, doi: 10.1186/s40814-017-0204-1.

[22] D. M. J. Milstein *et al.*, "Laser speckle contrast imaging identifies ischemic areas on gastric tube reconstructions following esophagectomy," *Med. (Baltimore)*, vol. 95, no. 25, Jun. 2016, Art. no. e3875, doi: 10.1097/MD.0000000000003875.

[23] G. L. Lu and B. W. Fei, "Medical hyperspectral imaging: A review," *J. Biomed. Opt.*, vol. 19, no. 1, Jan. 2014, doi: 10.1117/1.Jbo.19.1.010901.

[24] M. A. Calin *et al.*, "Hyperspectral imaging in the medical field: Present and future," *Appl. Spectrosc. Rev.*, vol. 49, no. 6, pp. 435–447, Aug. 2014, doi: 10.1080/05704928.2013.838678.

[25] N. T. Clancy *et al.*, "Surgical spectral imaging," *Med. Image Anal.*, vol. 63, Jul. 2020, Art. no. 101699, doi: 10.1016/j.media.2020.101699.

[26] K. J. Zuzak *et al.*, "Intraoperative bile duct visualization using near-infrared hyperspectral video imaging," *Amer. J. Surg.*, vol. 195, no. 4, pp. 491–497, Apr. 2008, doi: 10.1016/j.amjsurg.2007.05.044.

[27] L. van Manen *et al.*, "Feasibility of a snapshot hyperspectral imaging for detection of local skin oxygenation," in *Optical Biopsy XVII: Toward Real-Time Spectroscopic Imaging and Diagnosis*, San Francisco, CA, USA: SPIE, Mar. 2019, p. 25, doi: 10.1117/12.2507840.

[28] M. Barberio *et al.*, "Quantitative fluorescence angiography versus hyperspectral imaging to assess bowel ischemia: A comparative study in enhanced reality," *Surgery*, vol. 168, no. 1, pp. 178–184, Jul. 2020, doi: 10.1016/j.surg.2020.02.008.

[29] D. G. E. Thiem *et al.*, "Hyperspectral analysis for perioperative perfusion monitoring—A clinical feasibility study on free and pedicled flaps," *Clin. Oral Investigations*, Jun. 2020, doi: 10.1007/s00784-020-03382-6.

[30] B. Jansen-Winkeln *et al.*, "Determination of the transection margin during colorectal resection with hyperspectral imaging (HSI)," *Int. J. Colorectal Dis.*, vol. 34, no. 4, pp. 731–739, Apr. 2019, doi: 10.1007/s00384-019-03250-0.

[31] C. Caredda *et al.*, "Optimal spectral combination of a hyperspectral camera for intraoperative hemodynamic and metabolic brain mapping," *Appl. Sci.*, vol. 10, no. 15, Jul. 2020, Art. no. 5158, doi: 10.3390/app10155158.

[32] T. Wild *et al.*, "Hyperspectral imaging of tissue perfusion and oxygenation in wounds: Assessing the impact of a micro capillary dressing," *J. Wound Care*, vol. 27, no. 1, pp. 38–51, Jan. 2018, doi: 10.12968/jowc.2018.27.1.38.

[33] D. Yudovsky, A. Nouvong, and L. Pilon, "Hyperspectral imaging in diabetic foot wound care," *J. Diabetes Sci. Technol.*, vol. 4, no. 5, pp. 1099–1113, Sep. 2010, doi: 10.1177/193229681000400508.

[34] D. R. King *et al.*, "Surgical wound debridement sequentially characterized in a porcine burn model with multispectral imaging," *Burns*, vol. 41, no. 7, pp. 1478–1487, Nov. 2015, doi: 10.1016/j.burns.2015.05.009.

[35] N. T. Clancy *et al.*, "Dual multispectral and 3D structured light laparoscope," in *Proc. SPIE*, San Francisco, CA, USA, Mar. 2015, Art. no. 93160C, doi: 10.1117/12.2080346.

[36] J. M. Benavides *et al.*, "Multispectral digital colposcopy for in vivo detection of cervical cancer," *Opt. Exp.*, vol. 11, no. 10, pp. 1223–1236, May 2003, doi: 10.1364/Oe.11.001223.

[37] T. E. Renkoski, K. D. Hatch, and U. Utzinger, "Wide-field spectral imaging of human ovary autofluorescence and oncologic diagnosis via previously collected probe data," *J. Biomed. Opt.*, vol. 17, no. 3, Mar. 2012, doi: 10.1117/1.Jbo.17.3.036003.

[38] C. Zhang *et al.*, "A large, switchable optical clearing skull window for cerebrovascular imaging," *Theranostics*, vol. 8, no. 10, pp. 2696–2708, 2018, doi: 10.7150/thno.23686.

[39] K. J. Zuzak *et al.*, "Characterization of a near-infrared laparoscopic hyperspectral imaging system for minimally invasive surgery," *Anal. Chem.*, vol. 79, no. 12, pp. 4709–4715, Jun. 2007, doi: 10.1021/ac070367n.

[40] K. Mitra *et al.*, "Indocyanine-green-loaded microballoons for biliary imaging in cholecystectomy," *J. Biomed. Opt.,* vol. 17, no. 11, Nov. 2012, doi: 10.1117/1.Jbo.17.11.116025.

[41] S. G. Kong, M. E. Martin, and T. Vo-Dinh, "Hyperspectral fluorescence imaging for mouse skin tumor detection," *ETRI J.*, vol. 28, no. 6, pp. 770–776, Dec. 2006, doi: 10.4218/etrij.06.0106.0061.

[42] J. Cha *et al.*, "Real-time, label-free, intraoperative visualization of peripheral nerves and micro-vasculatures using multimodal optical imaging techniques," *Biomed. Opt. Exp.,* vol. 9, no. 3, pp. 1097–1110, Mar. 2018, doi: 10.1364/Boe.9.001097.

[43] S. Zhang *et al.*, "Multimodal imaging of cutaneous wound tissue," *J. Biomed. Opt.*, vol. 20, no. 1, Jan. 2015, Art. no. 016016, doi: 10.1117/1.JBO.20.1.016016.

[44] W. Ren *et al.*, "Quasi-simultaneous multimodal imaging of cutaneous tissue oxygenation and perfusion," *J. Biomed. Opt.*, vol. 20, no. 12, Sep. 2015, Art. no. 121307, doi: 10.1117/1.JBO.20.12.121307.

[45] A. Sdobnov *et al.*, "Combined multi-wavelength laser speckle contrast imaging and diffuse reflectance imaging for skin perfusion assessment," in *Proc. SPIE*, Munich, Germany, Jul. 2019, vol. 11075, Art. no. 110751F, doi: 10.1117/12.2526921.

[46] W. Feng, "Visualization of skin microvascular dysfunction of type 1 diabetic mice using in vivo skin optical clearing method," *J. Biomed. Opt.*, vol. 24, no. 3, pp. 1–9, Aug. 2018, doi: 10.1117/1.JBO.24.3.031003.

[47] S. M. White *et al.*, "Longitudinal *in vivo* imaging to assess blood flow and oxygenation in implantable engineered tissues," *Tissue Eng. Part C: Methods*, vol. 18, no. 9, pp. 697–709, Sep. 2012, doi: 10.1089/ten.tec.2011.0744.

[48] N. Mehta *et al.*, "Single-cell analysis using hyperspectral imaging modalities," *J. Biomechanical Eng.,* vol. 140, no. 2, Feb. 2018, doi: 10.1115/1.4038638.

[49] A. S. Luthman *et al.*, "Bimodal reflectance and fluorescence multispectral endoscopy based on spectrally resolving detector arrays," *J. Biomed. Opt.,* vol. 24, no. 3, Mar. 2019, doi: 10.1117/1.Jbo.24.3.031009.

[50] C. Zheng, L. W. Lau, and J. Cha, "Dual-display laparoscopic laser speckle contrast imaging for real-time surgical assistance," *Biomed. Opt. Exp.,* vol. 9, no. 12, pp. 5962–5981, Dec. 2018, doi: 10.1364/Boe.9.005962.

[51] L. Q. Kong *et al.*, "Non-contact detection of oxygen saturation based on visible light imaging device using ambient light," *Opt. Exp.*, vol. 21, no. 15, pp. 17464–17471, Jul. 2013, doi: 10.1364/Oe.21.017464.

[52] C.-I. Chang *et al.*, "A joint band prioritization and band-decorrelation approach to band selection for hyperspectral image classification," *IEEE. Trans. Geosci. Remote. Sens.*, vol. 37, no. 6, pp. 2631–2641, Nov. 1999.

[53] Y. Zhao *et al.*, "Optimal hemoglobin extinction coefficient data set for near-infrared spectroscopy," *Biomed. Opt. Exp.,* vol. 8, no. 11, pp. 5151–5159, Nov. 2017, doi: 10.1364/Boe.8.005151.

[54] M. Gawaz, "Role of platelets in coronary thrombosis and reperfusion of ischemic myocardium," *Cardiovasc. Res.*, vol. 61, no. 3, pp. 498–511, Feb. 2004, doi: 10.1016/j.cardiores.2003.11.036.

[55] V. Mazzaferro *et al.*, "Hepatic artery thrombosis after pediatric liver transplantation—A medical or surgical event?," *Transplantation,* vol. 47, no. 6, pp. 971–977, Jun. 1989, doi: 10.1097/00007890-198906000-00011.

[56] A. W. James, "Portomesenteric venous thrombosis after laparoscopic surgery: A systematic literature review," *Arch. Surg.*, vol. 144, no. 6, Jun. 2009, Art. no. 520, doi: 10.1001/archsurg.2009.81.

[57] L. Jafari-Saraf, S. E. Wilson, and I. L. Gordon, "Hyperspectral image measurements of skin hemoglobin compared with transcutaneous PO2 measurements," *Ann. Vasc. Surg.*, vol. 26, no. 4, pp. 537–548, May 2012, doi: 10.1016/j.avsg.2011.12.002.

[58] B. Lertsakdadet *et al.*., "Correcting for motion artifact in handheld laser speckle images," *J. Biomed. Opt.*, vol. 23, no. 3, pp. 1–7, Mar. 2018, doi: 10.1117/1.JBO.23.3.036006.

[59] L. Richards *et al.*, "Intraoperative laser speckle contrast imaging with retrospective motion correction for quantitative assessment of cerebral blood flow," *Neurophotonics*, vol. 1, no. 1, 2014, Art. no. 015006, doi: 10.1117/1.NPh.1.1.015006.